Numerical Reconstruction of Radiative Sources in an Absorbing and Nondiffusing Scattering Medium in Two Dimensions*

Hiroshi Fujiwara[†], Kamran Sadiq[‡], and Alexandru Tamasan[§]

Abstract. We consider the two dimensional quantitative imaging problem of recovering a radiative source inside an absorbing and scattering medium from knowledge of the outgoing radiation measured at the boundary. The medium has an anisotropic scattering property that is neither negligible nor large enough for the diffusion approximation to hold. We present the numerical realization of the authors' recently proposed reconstruction method. For scattering kernels of finite Fourier content in the angular variable, the solution is exact. The feasibility of the proposed algorithms is demonstrated in several numerical experiments, including simulated scenarios for parameters meaningful in optical molecular imaging.

Key words. transport equation, inverse problems, numerical source reconstruction, attenuated x-ray transform, attenuated Radon transform, scattering, A-analytic maps, Hilbert transform, Bukhgeim–Beltrami equation, optical molecular imaging

AMS subject classifications. $65N21,\ 30E20$

DOI. 10.1137/19M1282921

1. Introduction. We consider the inverse source problem for radiative transport in a bounded, strictly convex domain $D \subset \mathbb{R}^2$ with boundary ∂D , as modeled by the linearized Boltzmann equation. Let $S^1 = \{\xi \in \mathbb{R}^2 ; |\xi| = 1\}$ be the unit circle and $\Gamma_{\pm} := \{(x,\xi) \in \partial D \times S^1 ; \pm \nu(x) \cdot \xi > 0\}$ be the incoming (-), respectively, outgoing (+), unit tangent subbundles of the boundary, where $\nu(x)$ is the outer unit normal at $x \in \partial D$.

The medium is characterized by the absorption coefficient $\mu_{\mathbf{a}}(x)$, scattering coefficient $\mu_{\mathbf{s}}(x)$, and scattering kernel $p(x, \xi \cdot \xi')$, all of which are assumed known, real valued, nonnegative, essentially bounded functions. For any $x \in D$ and $\xi \in S^1$, the scattering kernel (a conditional probability) satisfies $\int_{S^1} p(x, \xi \cdot \xi') d\sigma_{\xi'} = 1$. The total attenuation is defined as $\mu_{\mathbf{t}} = \mu_{\mathbf{a}} + \mu_{\mathbf{s}}$.

Generated by an unknown source q, in the steady state case, and assuming no incoming radiation from outside the domain, the density of particles $I(x,\xi)$ at $x \in D$ traveling in the

^{*}Received by the editors August 22, 2019; accepted for publication (in revised form) January 13, 2020; published electronically March 31, 2020.

https://doi.org/10.1137/19M1282921

Funding: The work of the first author was supported by JSPS KAKENHI grants 16H02155, 18K18719, and 18K03436. The work of the second author was supported by the Austrian Science Fund (FWF) grant P31053-N32. The work of the third author was partially supported by the National Science Foundation grant DMS-1907097.

[†]Graduate School of Informatics, Kyoto University, Kyoto 606-8501, Japan (fujiwara@acs.i.kyoto-u.ac.jp).

[‡]Johann Radon Institute of Computational and Applied Mathematics (RICAM), Linz, Upper Austria, A-4040 (kamran.sadig@ricam.oeaw.ac.at).

[§]Department of Mathematics, University of Central Florida, Orlando, FL 32816-1364 (tamasan@math.ucf.edu).

direction ξ satisfies the problem

(1.1a)
$$\begin{aligned} \xi \cdot \nabla_x I(x,\xi) + \mu_{\mathbf{t}}(x) I(x,\xi) \\ &= \mu_{\mathbf{s}}(x) \int_{S^1} p(x,\xi \cdot \xi') I(x,\xi') d\sigma_{\xi'} + q(x), \quad (x,\xi) \in D \times S^1, \\ I(x,\xi) \mid_{\Gamma} &= 0. \end{aligned}$$

The unknown source q is assumed square integrable and compactly supported in D. Under the above assumptions on μ_a, μ_s, p , and q, the forward problem (1.1) is well posed [10], with a unique solution I in the space

$$\{f \in L^2(D \times S^1); (x,\xi) \mapsto \xi \cdot \nabla f(x,\xi) \in L^2(D \times S^1)\}.$$

For well-posedness results under various other assumptions, see [1, 8, 9, 22] and the generic result in [36].

For a given medium, i.e., μ_a , μ_s , and p are known, we consider the following inverse source problem: Determine q in D from the measurement

(1.2)
$$I(x,\xi) = I_{\text{measure}}(x,\xi), \quad (x,\xi) \in \Gamma_+,$$

of the directional outflow at the boundary. In the presence of scattering, this problem is equivalent to inverting a smoothing operator, and therefore it is ill-posed.

When $\mu_{\rm a}=\mu_{\rm s}=0$, this is the classical x-ray tomography problem of Radon [31], where q is to be recovered from its integrals along lines, a problem which is well understood both on its theoretical and numerical facets (see, e.g., [16, 18, 26] and references therein). For $\mu_{\rm a}\neq 0$ but $\mu_{\rm s}=0$, this is the problem of inversion of the attenuated x-ray transform in two dimensions, solved by different methods in [2] and [28]; see [4, 6, 19, 23, 24, 27] for later approaches and some numerical implementation.

The inverse source problem in a scattering media considered here, i.e., $\mu_s p \neq 0$, has also been considered under various limiting constraints (e.g., [5, 17, 20, 21, 34]) with a most general result showing that the source is uniquely and stably determined by the outflow in [36]. However, the numerical solutions for the inverse source problem based on the above mentioned results have yet to be realized.

In the special case of a weakly (anisotropic) scattering media, where $||1-p|| \ll 1$, one may recover the source by devising algorithms for the iterative method proposed in [5]. However, based on a perturbation argument of the nonscattering case in [28], the method does not extend to strongly anisotropic scattering media considered here. Moreover, even in the case of a weakly scattering media, the requirement of solving one forward problem (a computationally extensive procedure) at each iteration renders the method inefficient from an imaging perspective.

When only partial data is available, the only known source reconstruction result is in the recent work of Klibanov and collaborators in [35], where the domain is a slab and measurements are available on each side on a finite segment.

In here we present a numerical reconstruction method based on the authors' recent theoretical results in [14] and propose one algorithm to recover the radiative sources. As demonstrated

in the numerical experiments below, the algorithms can handle the quantitative imaging of sources in a nonsmall scattering medium that is far from diffusive approximation, with applications to optical molecular imaging [29, 30].

Key to the reconstruction method is the realization that any finite Fourier content in the angular variable of the scattering kernel splits the problem into a nonscattering one and a boundary value problem for a finite elliptic system. The role of the finite Fourier content has been independently recognized in [25]. However, in general, the scattering kernel does have an infinite Fourier content. Such is the case in the numerical experiments below, where we work with the ubiquitous (two dimensional version of) the Henyey–Greenstein kernel

(1.3)
$$p(x, \xi \cdot \xi') = p(\xi \cdot \xi') = \frac{1}{2\pi} \frac{1 - g^2}{1 - 2g\xi \cdot \xi' + g^2} \quad \text{for all } x \in D.$$

In (1.3) the parameter $0 \le g \le 1$ models a degree of anisotropy with g = 0 being the isotropic case and g = 1 being the ballistic case. In the proposed reconstruction we use an approximate scattering kernel obtained by truncating the Fourier modes in the angular variable. The error estimate in the data due to such truncation (see section 3 below) allows us to interpret the reconstruction as a minimum residual solution, where for a given a priori noise level, the degree of truncation dictates the number of significant Fourier modes. Moreover, we devise a locally optimal criterion for the choice of the order of this truncation, which is independent of the unknown source.

The theoretical method originated in Bukhgeim's theory of A-analytic functions developed in [7] to treat the nonattenuating case and in [2] for the absorbing but nonscattering case and extends the ideas in [32, 33] to the scattering case. One of the numerical results in the first experiment below has been announced in [14].

2. Preliminaries. In this section we establish notation, while presenting the basic ideas of the reconstruction in the nonscattering case. The presentation follows the authors' ideas in [14, 32, 33], while the notation is that used by practitioners in optical tomography, e.g., [3]. We also depart from the original notation in [7] (used so far in [14, 32, 33]) and work with the positive Fourier modes. This will allow for the natural indexing of sequences. For the analytical framework, which specifies the regularity of the coefficients and proves the appropriate convergence of the ensuing series, we refer to [14]. We identify points $x = (x_1, x_2) \in \mathbb{R}^2$ with their complex representative $z = x_1 + ix_2 \in \mathbb{C}$. The method considers the transport model (1.1) in the Fourier domain of the angular variable. For $\xi = \xi(\theta) = (\cos \theta, \sin \theta) \in S^1$, let

(2.1)
$$I(z,\xi) = \sum_{m \in \mathbb{Z}} I_m(z)e^{-im\theta}$$

be the Fourier series representation of I in the angular variable. From the analysis of the forward problem (e.g., [10]), for a square integrable source and essentially bounded coefficients, the solution I of (1.1) is at least square integrable in the angular variable and thus the series (2.1) is summable in L^2 sense. Moreover, since I is real valued, $I_{-m} = \overline{I_m}$ and the angular dependence is completely determined by the sequence of its nonnegative Fourier modes

$$D \ni z \mapsto \langle I_0(z), I_1(z), I_2(z), \ldots \rangle.$$

Similarly, let

$$p(z, \xi \cdot \xi') = \sum_{m \in \mathbb{Z}} p_m(z) e^{-im\tau}$$

be the Fourier series representation of the scattering kernel, where τ is the angle formed by ξ and $\xi' \in S^1$. We assume that $\theta \mapsto p(z, \cos(\theta))$ is uniformly in $z \in D$ sufficiently smooth, such that its Fourier coefficients p_n have sufficient decay in n for the convergence analysis of ensuing series; see such details in [14, 33]. Moreover, since $p(z, \cos \tau)$ is both real valued and even in τ , p_m are real valued and $p_m = p_{-m}$ for $m \in \mathbb{Z}$.

By introducing the Cauchy–Riemann gradients in the spatial domain $\partial = (\partial_{x_1} - i\partial_{x_2})/2$ and $\overline{\partial} = (\partial_{x_1} + i\partial_{x_2})/2$, the advection operator becomes $\xi \cdot \nabla_x = e^{-i\theta}\overline{\partial} + e^{i\theta}\partial$. A projection on the basis $\{e^{im\tau}\}$ in $L^2(0,2\pi)$ reduces the original transport equation (1.1a) to the infinite dimensional elliptic system

$$\overline{\partial} I_{-1}(z) + \partial I_1(z) + \mu_t(z)I_0(z) = 2\pi\mu_s(z)p_0(z)I_0(z) + q(z)$$

and

(2.2)
$$\overline{\partial} I_m(z) + \partial I_{m+2}(z) + \mu_t(z) I_{m+1}(z) = 2\pi \mu_s(z) p_{m+1}(z) I_{m+1}(z), \quad m \neq -1.$$

In particular, in the nonattenuated and nonscattering case (when $\mu_t \equiv 0 \equiv \mu_s$) the system corresponding to (2.2) is

(2.3)
$$\overline{\partial} J_m(z) + \partial J_{m+2}(z) = 0, \quad m \neq -1.$$

The system (2.3) was originally introduced (in a context more general than needed here) in [7], and it was shown that their solutions satisfy a Cauchy like integral formula, where the interior values in D are recovered from their boundary values. More precisely, for each $m \geq 0$ and each $z \in D$ fixed,

$$(2.4) J_m(z) = \frac{1}{2\pi i} \int_{\partial D} \frac{J_m(\zeta)}{\zeta - z} d\zeta + \frac{1}{2\pi i} \int_{\partial D} \left\{ \frac{d\zeta}{\zeta - z} - \frac{d\overline{\zeta}}{\overline{\zeta} - \overline{z}} \right\} \sum_{j=1}^{\infty} J_{m+2j}(\zeta) \left(\frac{\overline{\zeta} - \overline{z}}{\zeta - z} \right)^j.$$

In the absorbing and nonscattering case ($\mu_s = 0$ but $\mu_a \ge 0$) the system (2.2) becomes

(2.5)
$$\overline{\partial} I_m(z) + \partial I_{m+2}(z) + \mu_t(z) I_{m+1}(z) = 0, \quad m \neq -1.$$

The system (2.5) has been studied first in [2] and shown that an integrating operator can be found to reduce it to (2.3). We briefly describe the explicit construction of the integrating factor introduced in [12] and its convolution form in [32] to be used in our reconstruction algorithms below. For brevity assume that μ_a and μ_s are extended by zero outside the domain.

algorithms below. For brevity assume that μ_a and μ_s are extended by zero outside the domain. For $(x,\xi) \in \mathbb{R}^2 \times S^1$, let $\mathbf{D}[\mu_t](x,\xi) = \int_0^\infty \mu_t(x+t\xi) dt$ be the divergent beam transform, $\mathbf{R}[\mu_t](s,\xi) = \int_{-\infty}^\infty \mu_t(s\xi+t\xi^{\perp}) dt$ be the Radon transform, and $\mathbf{H}[f](s) = \frac{1}{\pi} \text{ p.v.} \int_{-\infty}^\infty \frac{f(t)}{s-t} dt$ be the Hilbert transform, where $\xi^{\perp} \in S^1$ denotes the counterclockwise rotation of ξ by $\pi/2$. Let us define

(2.6)
$$h[\mu_{t}](x,\xi) = \mathbf{D}[\mu_{t}](x,\xi) - \frac{1}{2}(I - i\mathbf{H})\mathbf{R}[\mu_{t}](x \cdot \xi^{\perp}, \xi^{\perp}),$$

where $\boldsymbol{HR}[\mu_{\mathrm{t}}](x \cdot \xi^{\perp}, \xi^{\perp}) = \boldsymbol{H}[\boldsymbol{R}[\mu_{\mathrm{t}}](\cdot, \xi^{\perp})](x \cdot \xi^{\perp}) = \frac{1}{\pi} \text{ p.v. } \int_{-\infty}^{\infty} \frac{\boldsymbol{R}[\mu_{\mathrm{t}}](t, \xi^{\perp})}{x \cdot \xi^{\perp} - t} dt$. While there are many possible such integrating factors to reduce the system (2.5) to (2.3), the key feature of the construction in [12] is the fact that all the negative modes of $\theta \mapsto h[\mu_t](x,\xi(\theta))$ (and thus of $e^{\pm h}$) vanish, as shown in [6, 12, 26]. Let $\{\alpha_k(x); k \in \mathbb{Z}_{\geq 0}\}$ and $\{\beta_k(x); k \in \mathbb{Z}_{\geq 0}\}$ be the corresponding sequences of the Fourier modes,

(2.7)
$$e^{-h[\mu_{t}](x,\xi)} = \sum_{k=0}^{\infty} \alpha_{k}(x)e^{ik\theta}, \quad e^{h[\mu_{t}](x,\xi)} = \sum_{k=0}^{\infty} \beta_{k}(x)e^{ik\theta}.$$

Then, as shown in [32, Lemma 4.1], if

(2.8)
$$J_m = \sum_{k=0}^{\infty} \alpha_k I_{m+k}, \quad m \ge 0,$$

where $\{I_m\}$ is a solution to (2.5), then $\{J_m\}$ is a solution of (2.3), and conversely, if

$$(2.9) I_m = \sum_{k=0}^{\infty} \beta_k J_{m+k},$$

where $\{J_m\}$ solves (2.3), then $\{I_m\}$ is a solution of (2.5). Moreover, the Cauchy problem for (2.3) (and thus for (2.5)) has at most one solution.

3. Reconstruction in the presence of scattering. We consider now the scattering case, when the scattering kernel p is of polynomial type in the angular variable, i.e.,

$$p(z, \cos \theta) = \sum_{m=-M}^{M} p_m(z)e^{im\theta} = p_0(z) + 2\sum_{m=1}^{M} p_m(z)\cos(m\theta),$$

where M is the degree of the polynomial. We stress that no smallness is assumed on the Fourier modes p_m for m = 0, ..., M.

In this case the transport equation (1.1a) reduces to the system

(3.1a)
$$\overline{\partial}I_{-1}^{(M)} + \partial I_{1}^{(M)} + \mu_{t}I_{0}^{(M)} = 2\pi\mu_{s}p_{0}I_{0}^{(M)} + q,$$

(3.1b)
$$\overline{\partial} I_{m}^{(M)} + \partial I_{m+2}^{(M)} + \mu_{t} I_{m+1}^{(M)} = 2\pi \mu_{s} p_{m+1} I_{m+1}^{(M)}, \qquad 0 \le m \le M-1,$$
(3.1c)
$$\overline{\partial} I_{m}^{(M)} + \partial I_{m+2}^{(M)} + \mu_{t} I_{m+1}^{(M)} = 0, \qquad m \ge M.$$

(3.1c)
$$\overline{\partial} I_m^{(M)} + \partial I_{m+2}^{(M)} + \mu_t I_{m+1}^{(M)} = 0, \qquad m \ge M$$

The basic idea in the reconstruction starts from the observation that the system (3.1c) is of the type (2.5). Therefore, via the integrating formulas (2.8) for $m \geq M$, the problem reduces to finding $\{J_m^{(M)}\}_{m\geq M}$ a solution of the Cauchy problem for the elliptic system (2.3). Moreover, from the data on the boundary (1.1b) and (1.2), we pose

$$I_{\mathrm{bd}}(\zeta,\xi) = \begin{cases} 0, & (\zeta,\xi) \in \Gamma_{-}; \\ I_{\mathrm{measure}}(\zeta,\xi), & (\zeta,\xi) \in \Gamma_{+}, \end{cases}$$

and we can recover for each $m \geq M$

$$I_m^{(M)}(\zeta) = \frac{1}{2\pi} \int_0^{2\pi} I_{\rm bd}(\zeta, \xi(\theta)) e^{im\theta} d\theta, \quad \zeta \in \partial D,$$

and by using (2.8) we find the boundary data

$$J_m^{(M)} \mid_{\partial D} = \sum_{k=0}^{\infty} \alpha_k I_{k+m} \mid_{\partial D}, \quad m \ge M.$$

Next we use the Cauchy-like integral formula (2.4) to recover the interior values $\{J_m(z); z \in D\}$ for $m \ge M$. Finally, we use (2.9) to recover the interior values $\{I_m(z); z \in D\}$,

$$I_m^{(M)} \mid_{\partial D} = \sum_{k=0}^{\infty} \beta_k J_{k+m} \mid_{\partial D} \quad m \ge M.$$

Recursively and in decreasing order starting with the index m = M - 1 to m = 0, we solve the elliptic problems (3.1b) as follows. By applying ∂ to (3.1b), we are lead to solving

(3.2a)
$$\Delta I_m^{(M)} = 4\partial \left\{ -\partial I_{m+2}^{(M)} + (2\pi\mu_s p_{m+1} - \mu_t) I_{m+1}^{(M)} \right\} \quad \text{in } D$$

while on the boundary

(3.2b)
$$I_m^{(M)}(\zeta) = \frac{1}{2\pi} \int_0^{2\pi} I_{\text{bd}}(\zeta, \xi(\theta)) e^{im\theta} d\theta, \qquad \zeta \in \partial D$$

for $0 \le m \le M-1$. This is the boundary value problem of the Poisson equation in D. Since $I_M^{(M)} \in H^1(D)$ the right-hand side of (3.2a) lies in $H^{-1}(D)$. Since the trace at the boundary is in $H^{1/2}(\partial D)$ the unique solution $I_{M-1}^{(M)} \in H^1(D)$, and thus the regularity requirement needed to carry the argument to the next index down is satisfied. Recursively, we recovered $I_{M-1}^{(M)}$, $I_{M-2}^{(M)}$, ..., and $I_0^{(M)}$ in D.

Finally, since $I_{-1}^{(M)} = \overline{I_1^{(M)}}$, from the recovered $I_1^{(M)}$ and $I_0^{(M)}$, we can now use (3.1a) to reconstruct the unknown source q in D.

Remark 3.1. In general, the scattering kernel p is not of polynomial type. An immediate application of the well posedness of the forward problem in $L^2(D \times S^1)$ gives an error estimate in the measured outflow due to the approximation in the scattering kernel.

Proposition 3.2. Let μ_t , μ_s , p be such that the forward problem (1.1) has a unique solution and let \tilde{p} be such that

$$\int_{D\times S^1} |p(x,\xi\cdot\xi') - \tilde{p}(x,\xi\cdot\xi')|^2 d\sigma_{\xi} dx \le \epsilon^2$$

for some $0 < \epsilon < 1$, and let \tilde{I} be the unique solution for (1.1) corresponding to \tilde{p} . Then,

(3.3)
$$||I|_{\Gamma_{+}} - \tilde{I}|_{\Gamma_{+}}|| \leq C\epsilon,$$

where C > 0 is a constant depending only on μ_t, μ_s, p , and the domain.

Proof. It is easy to see that the differences of the two corresponding solutions $h = I - \tilde{I}$ satisfy

$$\xi \cdot \nabla_x h + \mu_t h = \mu_s \int_{S^1} \tilde{p}h \, d\sigma_{\xi'} + \mu_s \int_{S^1} (\tilde{p} - p)I \, d\sigma_{\xi'},$$
$$h \mid_{\Gamma} = 0.$$

By interpreting the last term as a source and using the classical estimates in the forward model (see, e.g., [36, Theorem 2.1]), we obtain

$$||I|_{\Gamma_{+}} - \tilde{I}|_{\Gamma_{+}}||_{L^{2}(\Gamma_{+})} \leq \sup_{D} \mu_{s} ||\int_{D \times S^{1}} |(\tilde{p} - p)I| d\sigma_{\xi'} dx||$$

$$\leq \sup_{D} \mu_{s} ||I||_{L^{2}(D \times S^{1})} ||p - \tilde{p}||_{L^{2}(D \times S^{1})} \leq C\epsilon.$$

For the two dimensional Henyey–Greenstein kernel (1.3), with $0 \le g < 1$, considered in the numerical simulations

$$p(\xi \cdot \xi') = \frac{1}{2\pi} \frac{1 - g^2}{1 - 2g\xi \cdot \xi' + g^2} = \frac{1}{2\pi} \left(\sum_{m \in \mathbb{Z}} g^{|m|} e^{im\theta} \right)$$

and its Mth order truncation

(3.4)
$$p^{(M)}(\xi \cdot \xi') = \frac{1}{2\pi} \left(\sum_{|m| < M} g^{|m|} e^{im\theta} \right),$$

one obtains a refined estimate in terms of the anisotropic parameter g. Namely,

$$\int_{D\times S^1} |p(\xi \cdot \xi') - p^{(M)}(\xi \cdot \xi')|^2 d\sigma_{\xi} dx = \pi \int_{S^1} |p(\xi \cdot \xi') - p^{(M)}(\xi \cdot \xi')|^2 d\sigma_{\xi}$$
$$= \sum_{m=M+1}^{\infty} g^{2m} = \frac{g^{2M+2}}{1-g^2},$$

where the second last equality uses Parseval's identity.

For a given level of noise, a sufficiently large choice of M yields that the difference (3.3) between the exact data and the hypothetical data (which would be obtained had the scattering been of polynomial type) falls under the noise level. Therefore our reconstruction produces a source for which the corresponding boundary data is indistinguishable from the exact data within the level of noise. This is the most we can hope to reconstruct. It is worth noting that, for the scattering kernels of polynomial type, the method above does produce the exact solution in a stable manner, as shown by the authors in [14, Corollary 6.1].

4. Numerical implementations.

4.1. Evaluation of the Hilbert transform. An accurate calculation of the Hilbert transform is one of the crucial steps in our algorithm. This transform appears in computing the integrating factor in (2.6) and its Fourier modes in the angular variable (2.7). In order to perform a reliable numerical integration we need to properly account for the presence of the singularity in the kernel. The next simple lemma is key to our numerical treatment of the Hilbert transform.

Lemma 4.1. Suppose that $f \in C_0^1(\mathbb{R})$ and supp $f \subset [a,b]$. Then

$$\text{p.v.} \int_{-\infty}^{\infty} \frac{f(t)}{s-t} \, dt = \begin{cases} -\int_{a}^{b} g(s,t) \, dt + f(s) \log \frac{s-a}{b-s}, & s \in (a,b); \\ \int_{a}^{b} \frac{f(t)}{s-t} \, dt, & s \notin [a,b]; \\ \int_{a}^{b} g_{a}(t) \, dt, & s = a; \\ \int_{a}^{b} g_{b}(t) \, dt, & s = b, \end{cases}$$

where g, g_a , g_b are bounded and continuous functions defined by

$$g(s,t) = \begin{cases} \frac{f(s) - f(t)}{s - t}, & s \neq t; \\ f'(s), & s = t, \end{cases}$$

$$g_a(t) = \begin{cases} \frac{f(t)}{a - t}, & t > a; \\ 0, & t = a, \end{cases}$$

$$g_b(t) = \begin{cases} \frac{f(t)}{b - t}, & t < b; \\ 0, & t = b. \end{cases}$$

It means that the integrals on the right-hand side are those in the sense of Riemann.

Proof. First, for $s \in (a, b)$, then

$$\begin{aligned} \text{p.v.} \int_{-\infty}^{\infty} \frac{f(t)}{s-t} \, dt &= \lim_{\epsilon \downarrow 0} \bigg\{ - \int_{a}^{s-\epsilon} \frac{f(s) - f(t)}{s-t} \, dt + \int_{a}^{s-\epsilon} \frac{f(s)}{s-t} \, dt \\ &- \int_{s+\epsilon}^{b} \frac{f(s) - f(t)}{s-t} \, dt + \int_{s+\epsilon}^{b} \frac{f(s)}{s-t} \, dt \bigg\}, \end{aligned}$$

since $f \in C^1$ the function g(s,t) is bounded continuous function on \mathbb{R}^2 , and thus the calculation is followed by

$$\begin{split} &= -\int_a^b g(s,t) \ dt + f(s) \lim_{\epsilon \downarrow 0} \left\{ \int_a^{s-\epsilon} \frac{dt}{s-t} + \int_{s+\epsilon}^b \frac{dt}{s-t} \right\} \\ &= f(s) \log \frac{s-a}{b-s} - \int_a^b g(s,t) \ dt. \end{split}$$

Second, for $s \notin [a, b]$, the integrand of the transform $\frac{f(s)}{s-t}$ is regular as a function of $t \in [a, b]$. Finally, for s = a, then

p.v.
$$\int_{-\infty}^{\infty} \frac{f(t)}{a-t} dt = \lim_{\epsilon \downarrow 0} \left(\int_{-\infty}^{a-\epsilon} \frac{f(t)}{a-t} dt + \int_{a+\epsilon}^{\infty} \frac{f(t)}{a-t} dt \right)$$
$$= \lim_{\epsilon \downarrow 0} \int_{a+\epsilon}^{\infty} \frac{f(t)}{a-t} dt,$$

since $f(t) \equiv 0$ for $t < a - \epsilon$. By virtue of $f \in C^1$ and f(a) = f'(a) = 0, g_a is bounded and continuous on the interval $t \geq a$. Similar consideration works for the case s = b, which completes the proof.

Another choice of nonzero interval of f may give a different expression. For example, if we adopt $[a', b'] \supset [a, b]$, then

p.v.
$$\int_{-\infty}^{\infty} \frac{f(t)}{s-t} dt = f(s) \log \frac{s-a'}{b'-s} - \int_{a'}^{b'} g(s,t) dt$$
.

It is easily seen by calculation that both expressions are equivalent. Therefore we can theoretically choose any nonzero interval to evaluate the Hilbert transform as the Riemann integral of bounded and continuous functions.

For the case of a < s < b, we split the interval at s in numerical computation:

p.v.
$$\int_{-\infty}^{\infty} \frac{f(t)}{s-t} dt = f(s) \log \frac{s-a}{b-s} - \int_{a}^{s} g(s,t) dt - \int_{s}^{b} g(s,t) dt$$

because g(s,t) may not be smooth on t=s. It is also convenient to employ the midpoint rule in order to avoid implementation of f' appeared in g.

4.2. Computation of Cauchy-type integral formula. Assume that ∂D has a parameterization $\zeta(\omega),\ 0 \leq \omega < 2\pi,$ and D contains the origin for simplicity. Suppose that $0 = \omega_0 < \omega_1 < \cdots < \omega_{K-1} < \omega_K = 2\pi.$ Take $\zeta_k \in \partial D$ with $\operatorname{Arg} \zeta_k \in [\omega_k, \omega_{k+1}),$ where $\operatorname{Arg} \zeta \in [0, 2\pi)$ is the argument of $\zeta \in \mathbb{C}$. Let us consider the discretization of the complex integral of an integrable function $f(\zeta) = \sum_{k=0}^{K-1} f_k \Psi_k(\zeta)$ on ∂D , which is

$$\int_{\partial D} f(\zeta) d\zeta = \int_0^{2\pi} f(\zeta(\omega)) \zeta'(\omega) d\omega = \sum_{k=0}^{K-1} f_k \int_0^{2\pi} \Psi_k \circ \zeta(\omega) \zeta'(\omega) d\omega.$$

We consider two examples as Ψ_k . If $\Psi_k \circ \zeta$ is the characteristic function of the interval $[\omega_k, \omega_{k+1}]$, then the integral is approximated by

(4.1)
$$\int_{\partial D} f(\zeta) d\zeta = \sum_{k=0}^{K-1} f_k \int_{\omega_k}^{\omega_{k+1}} \zeta'(\omega) d\omega \approx \sum_{k=0}^{K-1} f_k \zeta_k'(\omega_{k+1} - \omega_k),$$

where ζ_k' is the derivative at a certain point in the interval $[\omega_k, \omega_{k+1})$. On the other hand, if one can choose $\Psi_k \circ \zeta$ to be the continuous and piecewise-linear function with $\Psi_k \circ \zeta(\omega_\ell) = \delta_{k\ell}$

(Kronecker's delta) and $\omega_k = \operatorname{Arg} \zeta_k$, then the trapezoidal rule gives an approximation as

$$\int_{\partial D} f(\zeta) d\zeta = \sum_{k=0}^{K-1} f_k \int_{\omega_{k-1}}^{\omega_{k+1}} \Psi_k(\zeta(\omega)) \zeta'(\omega) d\omega \approx \sum_{k=0}^{K-1} f_k \zeta_k' \frac{\operatorname{Arg} \zeta_{k+1} - \operatorname{Arg} \zeta_{k-1}}{2},$$

where $\zeta_k' = \zeta'(\omega_k)$, $\zeta_{-1} = \zeta_{K-1} - 2\pi$ and $\zeta_K = \zeta_0 + 2\pi$ by virtue of the periodicity.

For the purpose of numerical computation, we express the integral in the second term on the right-hand side of (2.4) as

$$\frac{1}{2\pi i} \int_{\partial D} \left(\frac{d\zeta}{\zeta - z} - \frac{d\overline{\zeta}}{\overline{\zeta} - \overline{z}} \right) F(\zeta) = \frac{1}{\pi} \int_{0}^{2\pi} \operatorname{Im} \left(\frac{\zeta'(\omega)}{\zeta(\omega) - z} \right) F(\zeta(\omega)) d\omega$$

with F being the series in (2.4).

4.3. Proposed algorithm. In this subsection, we present the numerical algorithm for the source reconstruction.

Suppose that μ_a , μ_s , and p on D are known. Assume that ∂D has a smooth parameterization $\zeta(\omega)$, $0 \le \omega < 2\pi$. Without loss of generality, we can assume that the domain D contains the origin. $I_{\text{bd}}(\zeta,\xi)$ on Γ_+ are sampled at $(\zeta_k,\xi(\theta_n))$, where $\zeta_0,\ldots,\zeta_{K-1}$ are K distinct points on ∂D , and $\theta_n = 2\pi n/N$. We assume that $0 \le \operatorname{Arg} \zeta_0 < \operatorname{Arg} \zeta_1 < \cdots < \operatorname{Arg} \zeta_{K-1} < 2\pi$.

STEP 1. Fix positive integers M and S. The integer S should be chosen sufficiently large, at least $S \geq M+3$. Let $\zeta_k' = \zeta'(\operatorname{Arg}\zeta_k)$, $0 \leq k < K$. Choose the segmentation $0 = \omega_0 < \omega_1 < \cdots < \omega_K = 2\pi$ so that $\operatorname{Arg}\zeta_k \in [\omega_k, \omega_{k+1})$. From the periodicity we assert that $\omega_{j+K} = \omega_j + 2\pi$, $j \in \mathbb{Z}$. We introduce an inscribed polygonal domain $D_h \approx D$ and take a triangulation $\mathcal{T} = \{\tau_\ell\}$ of D_h , i.e., each τ_ℓ is a triangular domain, $\tau_\ell \cap \tau_k = \emptyset$ if $\ell \neq k$, and $\overline{D_h} = \bigcup_\ell \overline{\tau_\ell}$. Let $P_1(\mathcal{T})$ denote the set of the piecewise linear continuous functions with respect to \mathcal{T} . We denote by V the set of vertices of \mathcal{T} .

STEP 2. Compute

$$\alpha_{s,k} = \frac{1}{N} \sum_{n=0}^{N-1} \exp\left(-h[\mu_t](\zeta_k, \xi(\theta_n))\right) e^{-is\theta_n}$$

and

$$\beta_{s,\ell} = \frac{1}{N} \sum_{n=0}^{N-1} \exp\left(h[\mu_t](z_\ell, \xi(\theta_n))\right) e^{-is\theta_n}$$

for $0 \le s \le S$, $0 \le k < K$, and $z_{\ell} \in V$. The function $h[\mu_t]$ is evaluated by the use of the midpoint rule as stated so far.

Step 3. Compute

$$\mathcal{I}_{m,k} = \frac{1}{N} \sum_{n=0}^{N-1} I_{\text{bd}}(\zeta_k, \xi(\theta_n)) e^{im\theta_n}$$

for $0 \le m \le S$ and $0 \le k < K$.

STEP 4. Compute

$$\mathcal{J}_{m,k} = \sum_{0 \le s.s + m \le S} \alpha_{s,k} \mathcal{I}_{s+m,k}$$

for $M \le m \le S$ and $0 \le k < K$.

Step 5. Compute $\mathcal{J}_m(z_\ell)$ for $M \leq m \leq S-2$ and $z_\ell \in V \cap D$, where

$$(4.2) \quad \mathcal{J}_{m}(z) = \frac{1}{2\pi i} \sum_{k=0}^{K-1} \frac{\zeta_{k}'}{\zeta_{k} - z} \mathcal{J}_{m,k} \Delta \omega_{k}$$

$$+ \frac{1}{\pi} \sum_{k=0}^{K-1} \left\{ \operatorname{Im} \left(\frac{\zeta_{k}'}{\zeta_{k} - z} \right) \right\} \left\{ \sum_{m+2 \le m+2j \le S} \mathcal{J}_{m+2j,k} \left(\frac{\overline{\zeta_{k}} - \overline{z}}{\zeta_{k} - z} \right)^{j} \right\} \Delta \omega_{k}$$

with $\Delta\omega_k = \omega_{k+1} - \omega_k$, implied by (4.1). We can change it to $\Delta\omega_k = (\operatorname{Arg}\zeta_{k+1} - \operatorname{Arg}\zeta_{k-1})/2$ if the piecewise-linear approximation to $J_m \mid_D$ is valid.

STEP 6. Compute $\mathcal{J}_m(\zeta_\ell)$ for $M \leq m \leq S$ and $\zeta_\ell \in V \cap \partial D$ by interpolating $\{\mathcal{J}_{m,k} ; 0 \leq k < K\}$ obtained in Step 4.

Step 7. For $z_{\ell} \in V$, compute

$$\mathcal{I}_M(z_\ell) = \sum_{0 \le s, s+M \le S-2} \beta_{s,\ell} \mathcal{J}_{s+M}(z_\ell)$$

and

$$\mathcal{I}_{M+1}(z_{\ell}) = \sum_{0 \le s, s+M+1 \le S-2} \beta_{s,\ell} \mathcal{J}_{s+M+1}(z_{\ell}).$$

STEP 8. For $m = M+1, M, \ldots, 1, 0$ (in descending order), find a piecewise linear continuous function $\mathcal{I}_m|_{\partial D} = \sum a_\ell \varphi_\ell$ by interpolating $\{\mathcal{I}_{m,k} : 0 \le k < K\}$ obtained in Step 3, where φ_ℓ is a periodic and piecewise linear continuous function on ∂D with $\varphi_\ell(v_k) = \delta_{\ell k}$ (Kronecker's delta), $v_k \in V \cap \partial D$. A more detailed example follows the algorithm description.

STEP 9. For m = M - 1, M - 2, ..., 1, 0 (in descending order), find an approximation $\mathcal{I}_m \in P_1(\mathcal{T})$ to $I_m \in H^1(D)$ by solving the Dirichlet problem of the Poisson equation (3.2) with the standard P_1 finite element method [11]. The variational formulation for (3.2) is approximated as follows: Find $\mathcal{I}_m \in P_1(\mathcal{T})$ with (3.2b) to satisfy

$$-\int_{D_h} \nabla \mathcal{I}_m \cdot \nabla \varphi \, dx = 4 \int_{D_h} \partial \left\{ -\partial \mathcal{I}_{m+2} + (2\pi \mu_{\rm s} p_m - \mu_{\rm t}) \mathcal{I}_{m+1} \right\} \varphi \, dx$$
$$= -4 \sum_{\tau \in \mathcal{T}} \int_{\tau} \left\{ -\partial \mathcal{I}_{m+2} + (2\pi \mu_{\rm s} p_m - \mu_{\rm t}) \mathcal{I}_{m+1} \right\} \partial \varphi \, dx$$

for any $\varphi \in P_1(\mathcal{T})$ with $\varphi|_{V \cap \partial D_h} = 0$.

First for m = M - 1, Steps 7 and 8 give \mathcal{I}_{M+1} and \mathcal{I}_{M} on the right-hand side at $z_{\ell} \in V$, which leads the interpretation $\mathcal{I}_{M+1}, \mathcal{I}_{M} \in P_{1}(\mathcal{T})$. Particularly, if $\mathcal{I}_{M+1}(x) = a_{\ell}x_{1} + b_{\ell}x_{2} + c_{\ell}$

on a triangle τ_{ℓ} , then $\partial \mathcal{I}_{M+1}|_{\tau_{\ell}} = (a_{\ell} - ib_{\ell})/2$. Similarly for the test function $\varphi \in \mathcal{P}_1(\mathcal{T})$, we can find $\partial \varphi$. The integration on the right-hand side can be evaluated by a Gauss-type numerical integration [11] on each triangle τ . Then we can obtain $\mathcal{I}_{m-1} \in P_1(\mathcal{T})$ by solving the linear system.

For m = M - 2, M - 3, ..., 1, 0, we can find approximations $\mathcal{I}_m \in P_1(\mathcal{T})$ similarly.

STEP 10. For each triangle $\tau_{\ell} \in \mathcal{T}$, let $\mathcal{I}_1|_{\tau_{\ell}} = a_{\ell}x_1 + b_{\ell}x_2 + c_{\ell}$. Then reconstruction of $q|_{\tau_{\ell}}$ is given by (3.1a) as

$$q_{\ell} = \operatorname{Re}(a_{\ell}) + \operatorname{Im}(b_{\ell}) + \left\{ \mu_{t}(z_{\ell}) - 2\pi \mu_{s}(z_{\ell}) p_{0}(z_{\ell}) \right\} \operatorname{Re}(\mathcal{I}_{0}(z_{\ell})).$$

This ends the algorithm.

In Step 8, there may be a mismatch between the measurement points on the boundary and vertices of the triangulation for reconstruction. We solve this mismatch by interpolating the data on formers. Below we detail an example.

Let us assume that $\sum_{k} \mathcal{I}_{m,k} \chi_{k}$ gives an interpolation of $\{\mathcal{I}_{m,k} ; 0 \leq k < K\}$, where χ_{k} is square integrable on ∂D . Then a_{1}, \ldots, a_{L} can be determined as its best approximation in the sense of least square

$$\min_{a_1,\dots,a_L} \left\| \sum_{\ell} a_{\ell} \varphi_{\ell} - \sum_{k} \mathcal{I}_{m,k} \chi_{k} \right\|_{L^{2}(\partial D)}.$$

It is clear that there exists a unique minimizer. In particular, if the D is the unit circle and the measurement points ζ_k are equispaced, then the minimizer satisfies the system of linear equations

$$\frac{2\pi}{L} \begin{pmatrix} \frac{2}{3} & \frac{1}{6} & 0 & \cdots & \frac{1}{6} \\ \frac{1}{6} & \frac{2}{3} & \frac{1}{6} & \cdots & 0 \\ & \ddots & \ddots & \ddots & \\ 0 & \cdots & \frac{1}{6} & \frac{2}{3} & \frac{1}{6} \\ \frac{1}{6} & 0 & \cdots & \frac{1}{6} & \frac{2}{3} \end{pmatrix} \begin{pmatrix} a_1 \\ a_2 \\ \vdots \\ a_{L-1} \\ a_L \end{pmatrix} = \begin{pmatrix} b_1 \\ b_2 \\ \vdots \\ b_{L-1} \\ b_L \end{pmatrix},$$

where

$$b_{\ell} = \sum_{k} \mathcal{I}_{m,k} \int_{0}^{2\pi} \chi_{k}(\theta) \varphi_{\ell}(\theta) d\theta.$$

Hence the boundary value is given by $\mathcal{I}_m(v_\ell) = a_\ell$. The similar strategy is applicable for Step 6.

4.4. A locally optimal truncation criterion. We give a criteria on the choice of M. In the proposed algorithm, \mathcal{I}_0 is obtained in complex values. On the other hand, the exact value of the zeroth Fourier mode I_0 is real-valued since I is so. Therefore the imaginary part of \mathcal{I}_0 comes as errors in reconstruction. It is reasonable to consider that the errors in the real and the imaginary part interact with each other. This observation leads a choice of M to minimize the imaginary part of I_0 , which is expected to reduce the error in the real part efficiently. Based on this consideration, we call M optimal which attains a local minimum of the imaginary part

(4.3)
$$E_{\text{imag}} = \left\{ \sum_{\tau \in \mathcal{T}} |\tau_{\ell}| \left\{ \mu_{t}(z_{\ell}) - 2\pi \mu_{s}(z_{\ell}) p_{0}(z_{\ell}) \right\}^{2} \left(\operatorname{Im} \mathcal{I}_{0}(z_{\ell}) \right)^{2} \right\}^{1/2},$$

where $|\tau_{\ell}|$ is the area of τ_{ℓ} and $\{\mu_{t}(z_{\ell})-2\pi\mu_{s}(z_{\ell})p_{0}(z_{\ell})\}$ Im $\mathcal{I}_{0}(z_{\ell})$ corresponds to the imaginary part of reconstructed q on τ_{ℓ} . In order to obtain an optimal M, we reconstruct the source for several values of M, then choose a value which minimizes E_{imag} . We stress here that the optimality indicator in (4.3) does not require knowledge of the unknown source.

5. Numerical experiments. In this section we demonstrate the numerical feasibility of the proposed algorithm for two numerical examples. All computations are processed with IEEE754 double precision arithmetic. In both numerical experiments, the measurement data is generated by solving the forward problem (1.1) by the piecewise-constant upwind approximation [13]. Therefore it is natural to use the characteristic function as the interpolation basis Ψ_k in subsection 4.2 and χ_k in Step 8. The triangulation is generated by FreeFem++ [15].

The scattering coefficient is $\mu_s \equiv 5$. Physically, It means that the particle scatters on average every 1/5 unit of length. Given that D is the unit disc, particles scatter on average 10 times before getting out. We use the two dimensional version of the Henyey–Greenstein scattering kernel in (1.3)

$$p(\xi \cdot \xi') = \frac{1}{2\pi} \frac{1 - g^2}{1 - 2g\xi \cdot \xi' + g^2}$$

with the anisotropy parameter g = 1/2. This choice is halfway between the ballistic g = 1 and isotropic g = 0 case. The Fourier expansion of the scattering kernel in (3.4)

$$\frac{1}{2\pi} \frac{1 - g^2}{1 - 2g\cos\theta + g^2} = \frac{1}{2\pi} \left(\sum_{m \in \mathbb{Z}} g^{|m|} e^{im\theta} \right)$$

yields the simple form of the modes $p_m = g^m/2\pi$ for all $m \ge 0$.

In the discretization of the boundary, we adopt S = 128, while for the midpoint rule in the computations of the integral transforms, we use 100 sampling points.

Experiment 5.1 (see [14]). Let

$$R = (-0.25, 0.5) \times (-0.15, 0.15),$$

$$B_1 = \{ (x_1, x_2) ; (x_1 - 0.5)^2 + x_2^2 < 0.3^2 \},$$

$$B_2 = \left\{ (x_1, x_2) ; (x_1 + 0.25)^2 + \left(x_2 - \frac{\sqrt{3}}{4} \right)^2 < 0.2^2 \right\}$$

be the rectangular, respectively, circular subsets of D as shown in Figure 1.

The source, to be reconstructed, is

(5.1)
$$q(x) = \begin{cases} 2 & \text{in } R; \\ 1 & \text{in } B_2; \\ 0 & \text{otherwise.} \end{cases}$$

The absorption coefficient $\mu_{\rm a}(x)$ is given by

$$\mu_{\mathbf{a}}(x) = \begin{cases} 2 & \text{in } B_1; \\ 1 & \text{in } B_2; \\ 0.1 & \text{otherwise.} \end{cases}$$

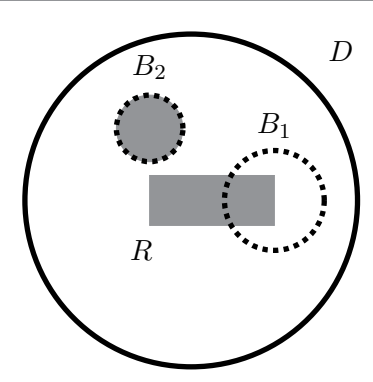


Figure 1. Locations of inclusions in numerical examples. The medium is relatively strongly absorbing inside the dotted balls, while the source q(x) is located in the gray regions.

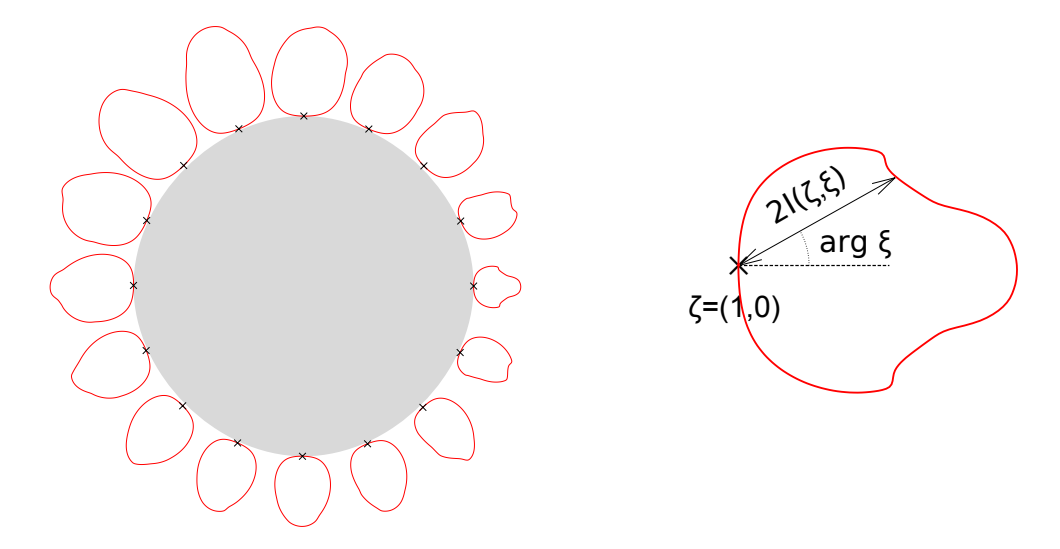


Figure 2. Boundary data $I_{bd}(\zeta,\xi)$ on $\partial D \times S^1$, obtained by the numerical computation of the forward problem in the unit disc (in grey). For $\zeta \in \partial D$ (indicated by \times), the red curve is $\{\zeta + 2I(\zeta,\xi)\xi; \xi \in S^1\}$ (on the left). The right figure is a magnification of the curve at $\zeta = (1,0)$.

To generate the measurement data I_{measure} in (1.2), which is the outflow on Γ_+ , we solve the forward problem using the numerical method in [13] with a triangular mesh of 5,542,718 triangles and 360 equispaced velocity intervals to describe the velocity directions. We disregard the value $I(x,\xi)$ of the solution for $x\in D$ and only keep the boundary values. The obtained data with (1.1b) is depicted in Figure 2. In this figure, for $x\in\partial D$ indicated by cross symbols (×), the graph of $\left(I(\zeta,\xi),\xi\right)$, $\xi\in S^1$, is shown by a red (closed) curve in the polar coordinate with the center at each ζ . In other words, the red curve is the graph of $\{\zeta+2I(\zeta,\xi)\xi;\xi\in S^1\}$ for $\zeta\in\partial D$ indicated by the cross symbols. By the assumption of no incoming radiation, i.e., $I|_{\Gamma_-}=0$, the red curve never appears inside |x|<1 indicated by gray in this expression.

To better exhibit the effect of scattering, in the second representation of the data $I|_{\Gamma_+}$ in Figure 3 we use the same coordinates as those used in a classical sinogram for the Radon

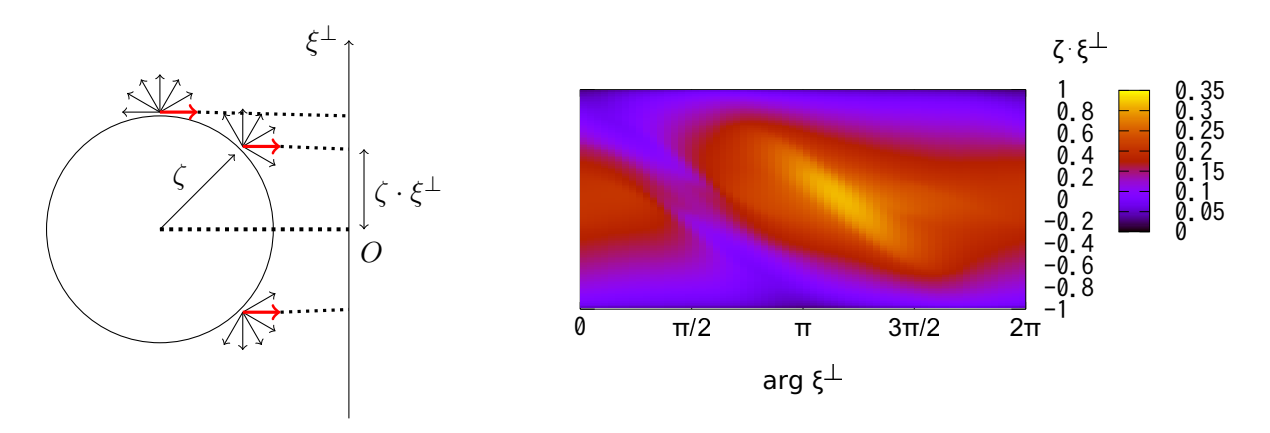


Figure 3. Left: Projection of the measurement data I_{measure} on Γ_+ . The red arrows, $I(\zeta,\xi)$ with $\xi = (1,0)$, are projected to the plane with $\text{Arg }\xi^{\perp} = \pi/2$. Right: Projection of I_{measure} on Γ_+ corresponding to Figure 2. The horizontal axis is the argument of the projection plane, and the vertical axis is the distance from the projected origin.

transform data. More precisely, the horizontal axis is the argument of the projection plane with direction ξ^{\perp} , while the vertical axis is the distance from the projected origin. In the absence of scattering, p=0, this representation would be exactly the sinogram for the attenuated Radon transform data. Note in Figure 3 how the scattering had combined and smeared out the features from the three locations of the source.

To avoid an inverse crime, the triangulation used in the reconstruction is different from that in the forward problem. In particular the reconstruction mesh consists of 6,998 triangles with 5,400 vertices (much less than the 5,542,718 triangles used in the forward problem) and is generated without any information of the location of the subsets R, B_1 , and B_2 . The computational time for reconstruction with M=6 is 340 seconds on Xeon E5-2650 v4 (2.2GHz, 12 cores) with OpenMP. Almost all computational time is occupied by the computation of the discrete Fourier transform of e^{-h} and e^{h} in Step 2, and the boundary integral (4.2) in Step 5, as 117 seconds, 79 seconds, and 141 seconds, respectively.

The reconstructed q(x) with M=6 is shown in Figure 4. Its cross sections along the dotted diameters $x_2 = -\sqrt{3}x_1$ and $x_2 = 0$, passing through the origin and the center of B_2 and R, respectively, are depicted in Figure 5. The reconstructed q(x) shows a quantitative agreement with the exact source in (5.1). Similar to the x-ray and attenuated X-ray tomography, the artifacts appear due to the co-normal singularities in the source but also in the attenuation.

Figure 6 shows the relation between M, errors in the corresponding imaginary part (4.3) (computed independent of q), and pseudoerrors (this requires knowledge of q) in the reconstructed q defined by

(5.2)
$$\left\{ \sum_{\tau_{\ell} : q \text{ is continuous}} |\tau_{\ell}| |q(z_{\ell}) - q_{\ell}|^2 \right\}^{1/2},$$

where $|\tau_{\ell}|$ is the area of τ_{ℓ} , z_{ℓ} is the center of the triangle τ_{ℓ} , and the summation runs over the triangles where q is continuous (in particular, constant in the example). From the figures,

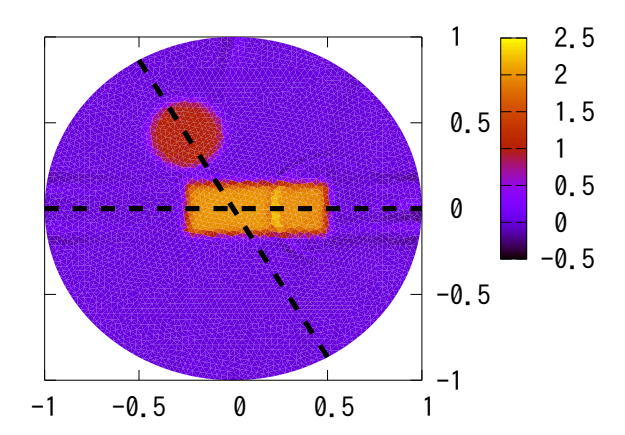


Figure 4. Reconstructed source with M=6.

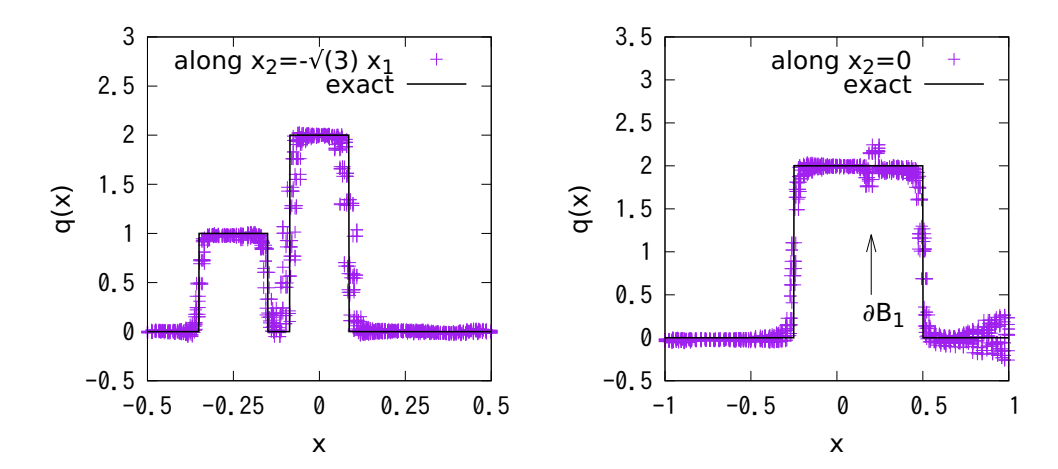


Figure 5. Section of the reconstructed source along the dotted lines in Figure 4, $|x_2 + \sqrt{3}x_1| < 0.05$ (on the left) and $|x_2| < 0.05$ (on the right), respectively. The arrow on the right figure indicate ∂B_1 where the scattering coefficient is discontinuous.

the error in the imaginary part scaled on the right axis is sufficiently smaller the pseudoerror scaled on the left axis. Both errors take minimum around M=5 and increase after that. More precisely, the error of the imaginary part (4.3) is minimum at M=6, while the pseudoerror of reconstructed q is minimum at M=3. According to the criteria stated before, we adopt M=6, which causes $|p_M| < 2.49 \times 10^{-3}$ in the setting.

Experiment 5.2. Let us consider the situation that μ_a is given by the modified Shepp-Logan phantom [37], which occupies the ellipse

$$D = \left\{ (x_1, x_2) \; ; \; \frac{x_1^2}{a^2} + \frac{x_2^2}{b^2} < 1 \right\}, \quad a = 0.69, b = 0.92.$$

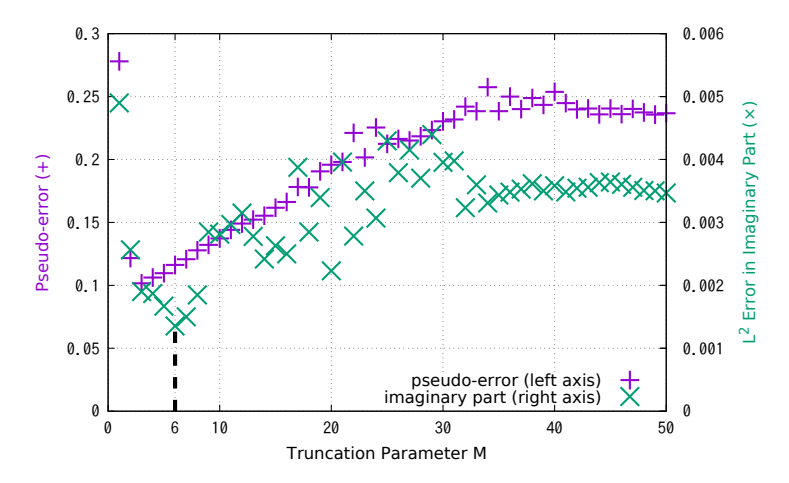


Figure 6. The truncation parameter M and pseudoerrors in reconstructed source $(+, left \ axis)$ and corresponding imaginary part $(\times, right \ axis)$ in Experiment 1.

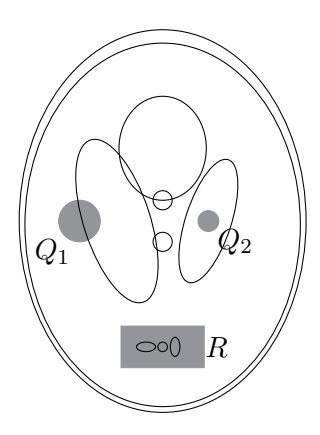


Figure 7. Discontinuous interface of μ_a (solid curves) in the Shepp-Logan phantom and the locations of support of the source q (gray).

We consider three disjoint domains in D (Figure 7),

$$Q_1 = \{ (x_1 + 0.4)^2 + x_2^2 < 0.1^2 \},$$

$$Q_2 = \{ (x_1 - 0.22)^2 + x_2^2 < 0.05^2 \},$$

$$R = \{ -0.2 < x_1 < 0.2, -0.705 < x_2 < -0.505 \},$$

and the internal source is given by

$$q(x) = \begin{cases} 2 & \text{in } Q_1 \cup Q_2; \\ 1 & \text{in } R; \\ 0 & \text{otherwise.} \end{cases}$$

The boundary measurement is generated by solving the forward problem with 1,554,282 triangles and 360 velocity directions, and is shown in Figure 8. The numbers of measurement

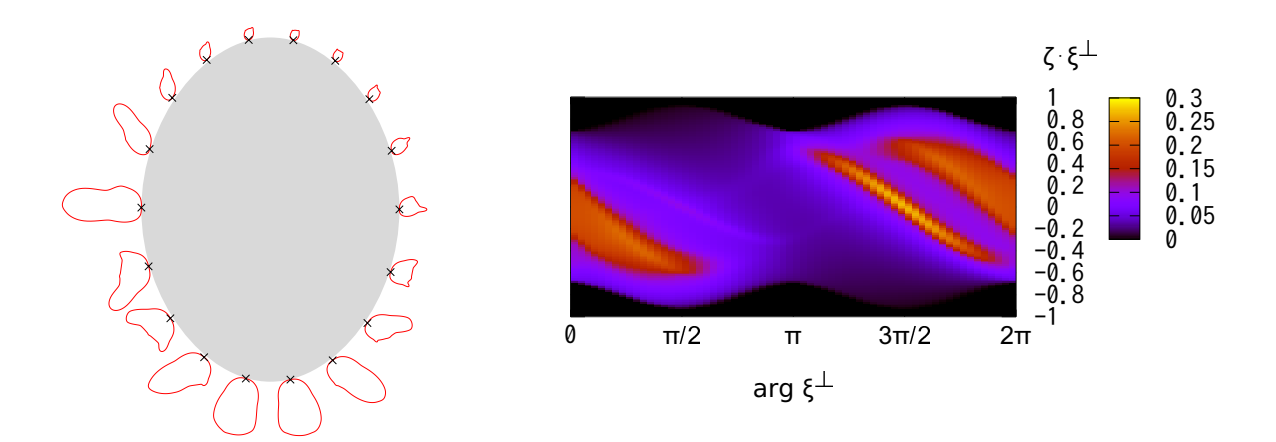


Figure 8. Boundary data $I_{\rm bd}$ on $\partial D \times S^1$ is shown by red curves, and the ellipse domain D is filled by gray (on the left), projection of measurement data $I_{\rm measure}$ on Γ_+ (on the right).

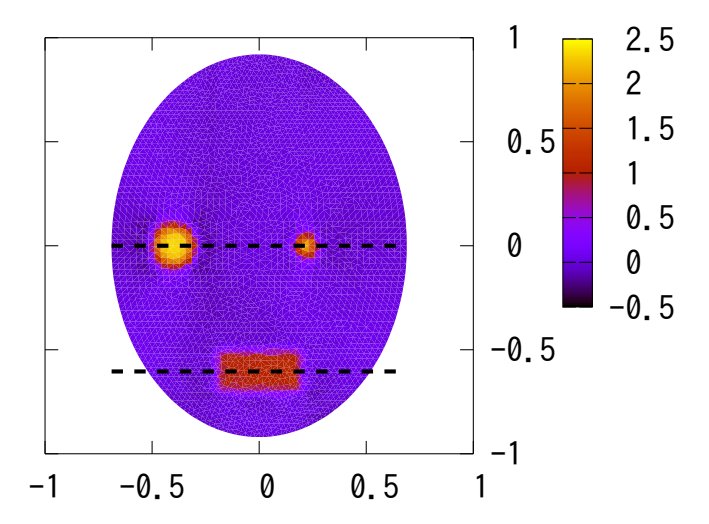


Figure 9. Numerical reconstruction of the source q(x) (real part) on D with M=8 in Experiment 2.

points are $K = 3{,}000$ on ∂D , and N = 360 on S^1 . On the contrary, the reconstruction mesh consists of 6,010 triangles with 3,106 vertices. Similarly as in the previous experiment, the latter mesh is generated without any information of μ_a and q. The boundary nodes on the ellipse generated by FreeFem++ are not equispaced with respect to their angles.

Figure 9 depicts the reconstructed q(x) on D with M=8, while Figure 10 is its sections on the dotted lines. The computational time for reconstruction with M=8 is 247 seconds on Xeon E5-2650 v4 (2.2GHz, 12 cores) with OpenMP. From the results, the support of q is clearly and quantitatively reconstructed, while the profile of μ_a does not appear.

The pseudoerrors in the reconstructed source and the errors of the corresponding imaginary part are shown in Figure 11. Our proposed optimality criterion yields to choose M=8 and M=40 as reasonable orders of truncation.

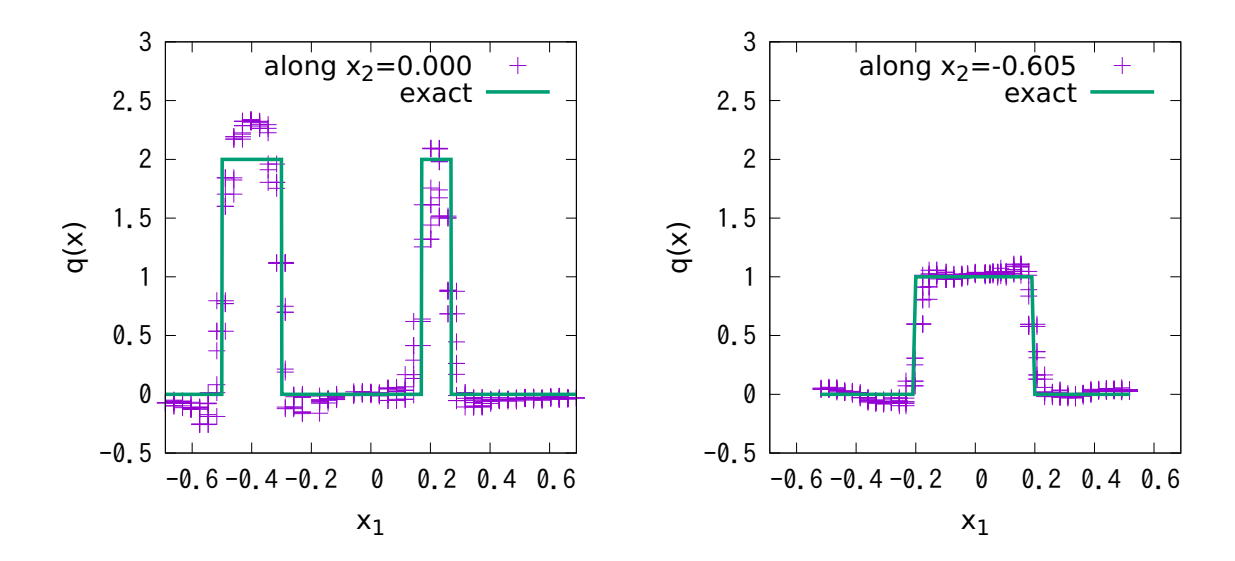


Figure 10. Cross sections of the reconstructed source q(x) with M=8 on the dotted lines in Figure 9, $|x_2| < 0.01$ (on left) and $|x_2 + 0.605| < 0.01$ (on right).

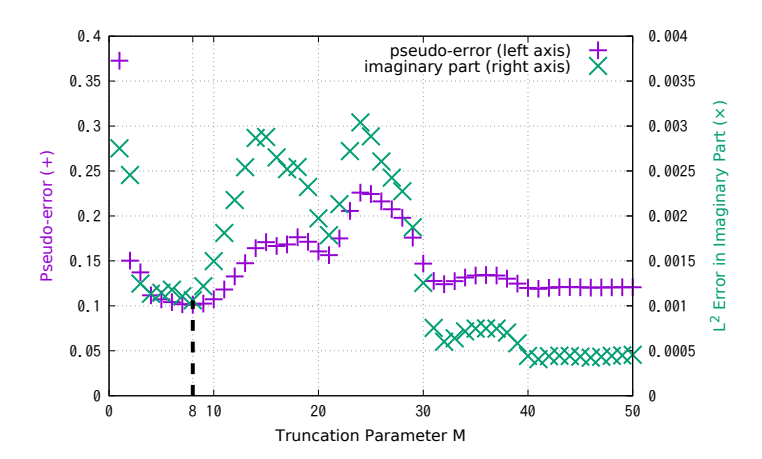
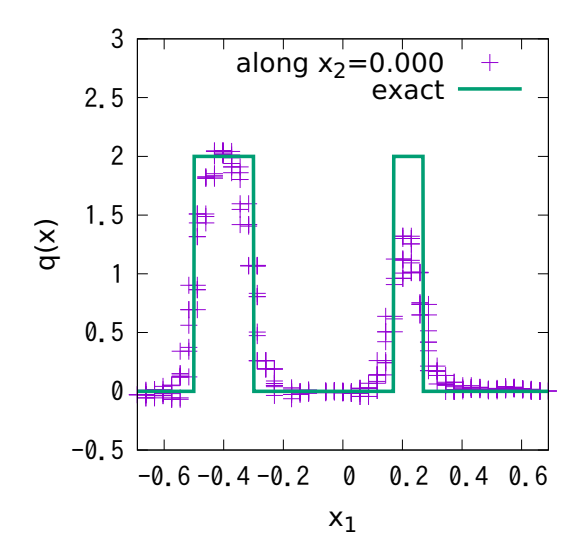


Figure 11. The truncation parameter M and pseudoerrors in reconstructed source (+, left axis) and corresponding imaginary part $(\times, right axis)$.

Figure 12 shows sections of the reconstructed q(x) with M=40 on the dotted lines in Figure 9. Although the value of (4.3) at M=40 is smaller than that at M=8, the peak of the source in Q_2 is not obtained well with M=40. The possible reason for this fact is that the size of Q_2 is small relative to the size of the triangular mesh, yielding that the discrete L^2 -norm used in computing the pseudoerror in (5.2) be less effective.

In general, the choice of an optimal truncation parameter M is not clear. However, our algorithm includes an optimality criterion which is independent of the knowledge of the source, thus making it feasible. The numerical experiments based on this choice were shown to produce accurate reconstructions.



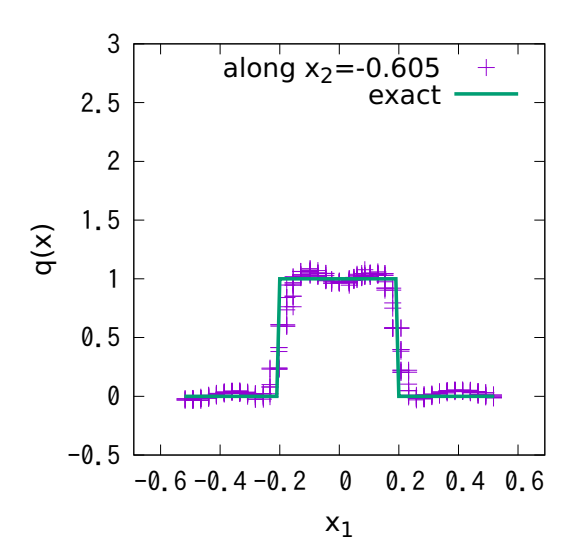


Figure 12. Cross sections of the reconstructed source q(x) with M=40 on the dotted lines in Figure 9, $|x_2| < 0.01$ (on left) and $|x_2 + 0.605| < 0.01$ (on right).

REFERENCES

- [1] D. S. ANIKONOV, A. E. KOVTANYUK, AND I. V. PROKHOROV, Transport Equation and Tomography, Inverse Ill-posed Probl. Ser. 30, VSP, Utrecht, 2002.
- [2] E. V. Arbuzov, A. L. Bukhgeĭm, and S. G. Kazantsev, Two-dimensional tomography problems and the theory of A-analytic functions, Siberian Adv. Math., 8 (1998), pp. 1–20.
- [3] S. R. Arridge, Optical tomography in medical imaging, Inverse Problems, 15 (1999), pp. R41–R93.
- [4] G. Bal, On the attenuated Radon transform with full and partial measurements, Inverse Problems, 20 (2004), pp. 399-418.
- [5] G. Bal and A. Tamasan, Inverse source problems in transport equations, SIAM J. Math. Anal., 39 (2007), pp. 57–76.
- [6] J. Boman and J.-O. Strömberg, Novikov's inversion formula for the attenuated Radon transform—A new approach, J. Geom. Anal., 14 (2004), pp. 185–198.
- [7] A. L. Bukhgeim, Inversion formulas in inverse problems, in Linear Operators and Ill-Posed Problems, Plenum, New York, 1995, pp. 323–378.
- [8] M. Choulli and P. Stefanov, Inverse scattering and inverse boundary value problems for the linear Boltzmann equation, Comm. Partial Differential Equations, 21 (1996), pp. 763–785.
- [9] M. CHOULLI AND P. STEFANOV, An inverse boundary value problem for the stationary transport equation, Osaka J. Math., 36 (1999), pp. 87–104.
- [10] R. DAUTRAY AND J.-L. LIONS, Mathematical Analysis and Numerical Methods for Science and Technology, Integral Equations and Numerical Methods, Springer-Verlag, Berlin, 1990.
- [11] A. ERN AND J.-L. GUERMOND, Theory and Practice of Finite Elements, Appl. Math. Sci. 159, Springer-Verlag, Berlin, 2004.
- [12] D. V. FINCH, The attenuated X-ray transform: Recent developments, in Inside Out: Inverse Problems and Applications, Math. Sci. Res. Inst. Publ. 47, Cambridge University Press, Cambridge, 2003, pp. 47–66.
- [13] H. Fujiwara, Piecewise constant upwind approximations to the stationary radiative transport equation, accepted, in Proceedings of International Conference Continuum Mechanics Focusing on Singularities, 2018.

- [14] H. FUJIWARA, K. SADIQ, AND A. TAMASAN, A Fourier approach to the inverse source problem in an absorbing and anisotropic scattering medium, Inverse Problems, 36 (2020), 015005.
- [15] F. Hecht, New development in freefem++, J. Numer. Math., 20 (2012), pp. 251-265.
- [16] S. HELGASON, The Radon Transform, Progr. Math. 5, Birkhäuser, Boston, MA, 1980.
- [17] M. Hubenthal, An inverse source problem in radiative transfer with partial data, Inverse Problems, 27 (2011), 125009.
- [18] P. KUCHMENT, *The Radon Transform and Medical Imaging*, CBMS-NSF Regional Conf. Ser. in Appl. Math. 85, SIAM, Philadelphia, 2014.
- [19] L. A. Kunyansky, A new SPECT reconstruction algorithm based on the Novikov explicit inversion formula, Inverse Problems, 17 (2001), pp. 293–306.
- [20] E. W. LARSEN, The inverse source problem in radiative transfer, J. Quant. Spectrosc. Radiat. Transf., 15 (1975), pp. 1–5.
- [21] N. J. MCCORMICK AND R. SANCHEZ, Solutions to an inverse problem in radiative transfer with polarization—II, J. Quant. Spectrosc. Radiat. Transf., 30 (1983), pp. 527–535.
- [22] M. Mokhtar-Kharroubi, Mathematical Topics in Neutron Transport Theory, Ser. Adv. Math. Appl. Sci., World Scientific, Singapore, 1997.
- [23] F. Monard, Efficient tensor tomography in fan-beam coordinates, Inverse Probl. Imaging, 10 (2016), pp. 433–459.
- [24] F. Monard, Efficient tensor tomography in fan-beam coordinates, II: Attenuated transforms, Inverse Probl. Imaging, 12 (2018), pp. 433–460.
- [25] F. Monard and G. Bal, Inverse Source Problems in Transport via Attenuated Tensor Tomography, https://arxiv.org/abs/arXiv:1908.06508v1, 2019.
- [26] F. NATTERER, The Mathematics of Computerized Tomography, John Wiley & Sons, Chichester, UK, 1986.
- [27] F. NATTERER, Inversion of the attenuated radon transform, Inverse Problems, 17 (2001), pp. 113–119.
- [28] R. G. NOVIKOV, Une formule d'inversion pour la transformation d'un rayonnement X atténué, C. R. Acad. Sci. Paris Sér. I Math., 332 (2001), pp. 1059–1063.
- [29] V. NTZIACHRISTOS AND R. WEISSLEDER, Experimental three-dimensional fluorescence reconstruction of diffuse media by use of a normalized Born approximation, Opt. Lett., 26 (2001), pp. 893–895.
- [30] V. NTZIACHRISTOS, A. G. YODH, M. SCHNALL, AND B. CHANCE, Concurrent MRI and diffuse optical tomography of breast after indocyanine green enhancement, Proc. Natl. Acad. Sci. USA, 97 (2000), pp. 2767–2772.
- [31] J. RADON, On the determination of functions from their integral values along certain manifolds, IEEE Trans. Med. Imaging, MI-5 (1986), pp. 170–176.
- [32] K. Sadiq and A. Tamasan, On the range characterization of the two-dimensional attenuated Doppler transform, SIAM J. Math. Anal., 47 (2015), pp. 2001–2021.
- [33] K. Sadiq and A. Tamasan, On the range of the attenuated Radon transform in strictly convex sets, Trans. Amer. Math. Soc., 367 (2015), pp. 5375–5398.
- [34] C. E. Siewert, An inverse source problem in radiative transfer, J. Quant. Spectrosc. Radiat. Transf., 50 (1993), pp. 603–609.
- [35] A. V. SMIRNOV, M. V. KLIBANOV, AND L. H. NGUYEN, On an inverse source problem for the full radiative transfer equation with incomplete data, SIAM J. Sci. Comput., 41 (2019), pp. B929–B952.
- [36] P. Stefanov and G. Uhlmann, An inverse source problem in optical molecular imaging, Anal. PDE, 1 (2008), pp. 115–126.
- [37] P. A. Toft, The Radon Transform—Theory and Implementation, PhD thesis, Technical University of Denmark, 1996.